Mixed-element USM3D Contributions to the 4th AIAA High-Lift Prediction Workshop

Michael D. Bozeman Jr.,* Mohagna J. Pandya,† and Michael A. Park‡
NASA Langley Research Center,
Hampton, VA 23681, USA

This paper discusses results of the mixed-element USM3D (USM3D-ME) simulations performed for the 4th AIAA High-Lift Prediction Workshop. The workshop was separated into six Technical Focus Groups to investigate the impact of geometry modeling, grid, and computational methods for predicting high-lift flows. This work was performed under the Fixed Grid Reynolds-averaged Navier-Stokes (RANS) Technical Focus Group. The primary geometry selected for the workshop was the High-Lift Common Research Model. The performed simulations included a flap deflection study and both a grid refinement study and pitch sweep for the nominal flap deflection configuration. The results show that USM3D-ME RANS solutions, generally, tends to underpredict the lift coefficient and to predict a less negative pitching moment relative to the experimental data. The predicted drag coefficient values agree better with experiment for smaller angles of attack but were observed to be larger than experiment for the largest angle of attack simulated. The results of the grid refinement study demonstrated a lack of grid convergence for the provided grid family. The results of the grid refinement study are consistent with the submissions to the Fixed Grid and Mesh Adaptation Technical Focus Groups. Grid convergence for the provided grid family remains elusive for the international community. A 2D Multielement Airfoil configuration was included to enable a turbulence model verification study, which illustrated favorable agreement between USM3D-ME and the solutions provided by other flow solvers.

I. Nomenclature

Acronyms

2DMEA	=	Two-dimensional, Multielement Airfoil
CFD	=	Computational Fluid Dynamics
CFL	=	Courant-Friedrichs-Lewy number
CRM-HL	=	High Lift Common Research Model
HLPW	=	High Lift Prediction Workshop
LES	=	Large Eddy Simulation
MAC	=	Mean Aerodynamic Chord
MRC	=	Moment Reference Center
QCR	=	Quadratic Constitutive Relation
RANS	=	Reynolds-averaged Navier-Stokes
SA	=	Spalart-Allmaras one-equation turbulence model
TFG	=	Technical Focus Group

*Research Aerospace Engineer, Configuration Aerodynamics Branch, Member AIAA.
†Research Aerospace Engineer, Configuration Aerodynamics Branch, Senior Member AIAA.
‡Research Scientist, Computational AeroSciences Branch, Senior Member AIAA.

Variable Names

C_L	=	Lift coefficient
C_D	=	Drag coefficient
C_m	=	Pitching moment coefficient
L/D	=	Lift-to-drag ratio
N	=	Number of cells
Re_{MAC}	=	Reynolds number based on mean aerodynamic chord
x, y, z	=	Coordinate axes

II. Introduction

THE 4th AIAA High-Lift Prediction Workshop (HLPW4) was held in conjuction with the 2022 AIAA SciTech Forum. The workshop focused on an assessment of the current state of the art for accurate predictions of high-lift flows, which feature possible unsteadiness, separated flow, and vortical flow due to both large angles of attack and high-lift devices such as leading-edge slats and trailing-edge flaps [1]. Based on these challenges, the HLPW workshop series was developed to advance the current state of the art with the following long-term objectives: 1) assess the numerical prediction capability (mesh, numerics, turbulence modeling, high-performance computing, etc.) of current-generation CFD technology for swept, medium/high-aspect ratio wings in landing/takeoff (high-lift) configurations, 2) develop practical modeling guidelines for CFD prediction of high-lift flowfields, 3) advance the understanding of the high-lift flow physics to enable development of more accurate prediction methods and tools, 4) enhance CFD prediction capability for practical high-lift aerodynamic design and optimization, 5) provide an impartial forum for evaluating the effectiveness of existing computer codes and modeling techniques, and 6) identify areas needing additional research and development [2].

The selected configuration for HLPW4 was the High-Lift Common Research Model (CRM-HL) model. The CRM-HL with flow-through nacelle and slat/flap support hardware [3] is the shared test case for all Technical Focus Groups (TFGs). A QinetiQ 5m pressurized low-speed wind tunnel test was conducted in preparation for the workshop [4], which defines the flap angles, flap gaps, flap overlaps, slat height, and slat gap used in HLPW-4.

The workshop [5] was separated into six TFGs to investigate the impact of geometry modeling, grid, and computational methods for predicting high-lift flows. Participants were allowed to contribute to as many TFGs as desired, with each TFG requiring a separate data submission. This paper focuses on CFD simulations performed for the Fixed Grid Reynolds-averaged Navier-Stokes (RANS) TFG [6] using the mixed-element USM3D (USM3D-ME) flow solver. Results are presented for the Mesh Adaptation for RANS TFG [7] as a secondary objective. The analyses performed include a flap deflection study, a grid refinement study including a solution adaptive-grid simulation, a pitch sweep, and a turbulence model study. Additionally, a turbulence model verification exercise was performed for a 2D multielement airfoil, which corresponds to an outboard slice of the CRM-HL wing. The following sections will discuss the simulation details, provided grids, and computational results along with comparisons to experimental data, when available, for additional insight.

III. Computational Methods

The computational methods employed are described in this section. The provided discussion includes descriptions of the flow solver, grid adaptation method, geometries, workshop provided grids, and test cases considered.

A. Mixed-element USM3D Flow Solver

USM3D is an unstructured-grid, cell-centered, Navier-Stokes solver developed at the NASA Langley Research Center as part of the Tetrahedral Unstructured Software System (TetrUSS) [8, 9]. Since its original introduction, USM3D has been extended for compatibility with mixed-element grids featuring tetrahedral, prismatic, pyramidal, and hexahedral elements [10] along with other enhancements to improve robustness and time to solution. The updated version of the code is referred to as USM3D-ME in this paper. One significant enhancement added to the code is the Hierarchical Adaptive Nonlinear Iteration Method (HANIM), which has been shown to be beneficial for some problems through improved robustness, accelerated convergence, and automation [11]. The automation offered by HANIM includes a Courant-Friedrichs-Lewy (CFL) number adaptation capability, which automatically adjusts the CFL number

based on the current state of the solution. This can potentially increase the convergence rate and does not require CFL input from the user. For this work, the inviscid terms were computed using Roe's flux difference splitting [12] without a flux limiter. The primary method for turbulent closure was the one-equation Spalart-Allmaras model with negative provisions [13]. This model is referred to as the SA-neg model for the remainder of this paper. Additionally, a turbulence model study was performed using the one-equation Spalart-Allmaras model with negative provisions, the rotation correction [14], and the Quadratic Constitutive Relation (QCR-2000) [15] for computing the Reynolds stresses. Finally, HANIM was used for all simulations presented in this paper.

B. Unstructured Grid Adaptation

The grid adaptation method employed for this work is discussed in this subsection with an overview provided by Kleb et al. [16]. Starting with an initial grid that conforms to the geometry [17], a flow solution is computed. The boundary representation tolerances present in the CRM-HL geometric model are accommodated [18]. The information from the flow solution is used to estimate error and specifies a new grid resolution and orientation request (metric field). The metric is constructed based on the Hessian of the Mach number and the complexity, proportional to the total number of vertices in the adapted grid, is computed. The metric is globally scaled to set its complexity to a requested value. The current grid is modified using the *refine* grid adaptation mechanics package [19] to conform to the specified metric. The previous CFD solution is interpolated to this new grid to form an initial condition for the flow solve on the new mesh.

A new flow solution is computed and the grid is further modified using *refine*. This process is repeated until exit criteria are met (e.g., accuracy requirement, resource limit). This process has been verified through comparison of independent implementations of the mesh automation process. For example, verification exercises for analytic functions [20], a wing in transonic flow [21], and a multielement airfoil [22] have been completed. These verified mesh adaptation methods have been applied to HLPW-3 [23] and HLPW-3 configurations after the workshop [24–28].

For this work, 10,000 flow solver iterations were performed for each grid. *refine* was used to modify the grid until the change in drag coefficient was below 0.1% over the last three grids. Once this was achieved, the complexity was doubled, which approximately doubles the number of vertices in the grid before employing *refine* for further modification. The complexity scheduling algorithm is a simplification of Alauzet and Frazza [29].

C. Geometry

The primary geometry for HLPW4 was the semispan, 10% scale CRM-HL configuration, featuring leading-edge slats and trailing-edge flaps. This model was tested in the QinetiQ 5m pressurized low-speed wind tunnel [3]. The test was performed over a range of angles of attack for various model configurations corresponding to takeoff and landing. The nominal landing configuration was selected for HLPW4, which consists of 30° leading-edge slat deflection and inboard/outboard trailing-edge flap deflections of 40°/37°, respectively. An illustration of the model is provided in Figure 1 along with technical specifications provided in Table 1.

Table 1 Technical Specifications for CRM-HL Geometry.

Mean Aerodynamic Chord (MAC)	275.8 in
Semispan Reference Area	297,360 in^2
Moment Reference Center (MRC)	x = 1325.9 in, y = 0.0 in, z = 177.95 in
Flap Deflection (inboard/outboard)	37°/34°, 40°/37°(nominal), 43°/40°
Slat Deflection (inboard/outboard)	30°/30°

In addition to the analyses performed for the CRM-HL, a two-dimensional, multielement airfoil was also analyzed for a turbulence model verification study. This geometry is referred to as the 2DMEA configuration for the remainder of this paper. The airfoil is a chordwise cross-section of the CRM-HL wing, which passes through the outboard slat and flap for the nominal landing configuration. The turbulence model verification study was requested from participants using codes that are not already represented in the results provided on the Turbulence Modeling Resource (TMR) website [30]. The goal was to verify that the implementation of the one-equation SA model in each participating code provided consistent results for the provided grids and solver settings. An illustration of the 2DMEA geometry is provided in Figure 2 along with technical specifications provided in Table 2.

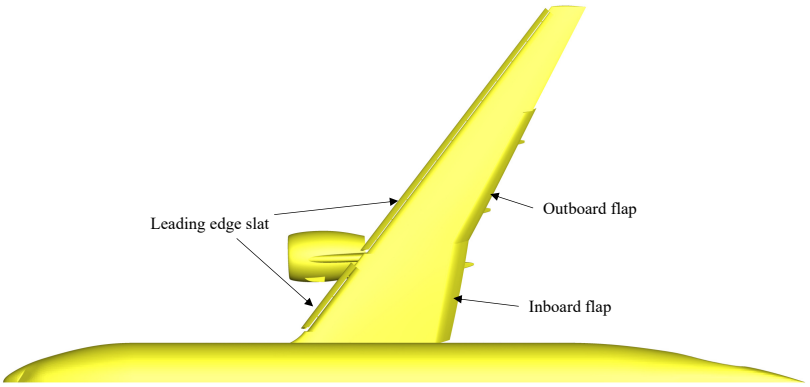

(a) Top view.

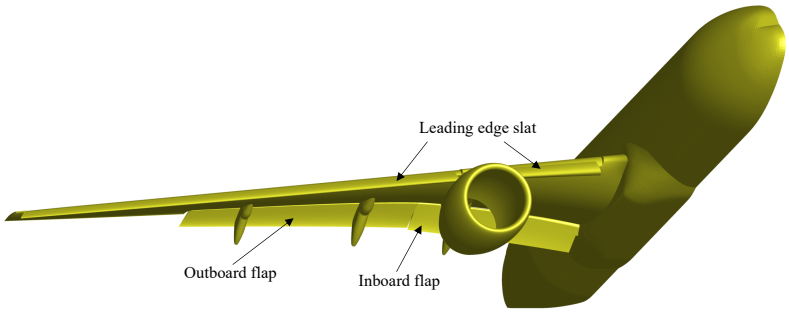

(b) Perspective view.

Fig. 1 CRM-HL geometry for HLPW4.

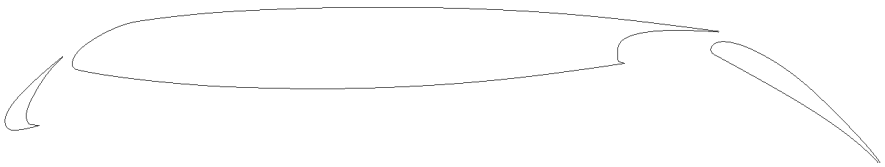

Fig. 2 2DMEA Geometry.

D. Grids

For the CRM-HL configuration, the workshop participants were provided with multiple sets of grids to choose from based on user preferences and solver capabilities. The grid types included structured overset, unstructured high-order, unstructured all-tetrahedral, and unstructured mixed-element grids. Additionally, a smoothed version of the unstructured grid families were provided, which were the original grids that had been post-processed using a smoothing algorithm [31]. For this work, the smoothed, all-tetrahedral grid family was used. Note that USM3D-ME is compatible with mixed-element grids. However, for this application, as compared to the mixed-element grids, the all-tetrahedral grids provided better iterative convergence. An illustration of the surface resolution of the smoothed, all-tetrahedral grids is provided in Figure 3. Finally, the sizes of the tetrahedral grids are described in Table 3.

Table 2 Technical Specifications for 2DMEA Geometry.

Mean Aerodynamic Chord (MAC)	1.0 in
Reference Area	1.0 in^2
Moment Reference Center (MRC)	x = 0.25 in, y = 0.0 in, z = 0.0 in
Flap Deflection	37°
Slat Deflection	30°

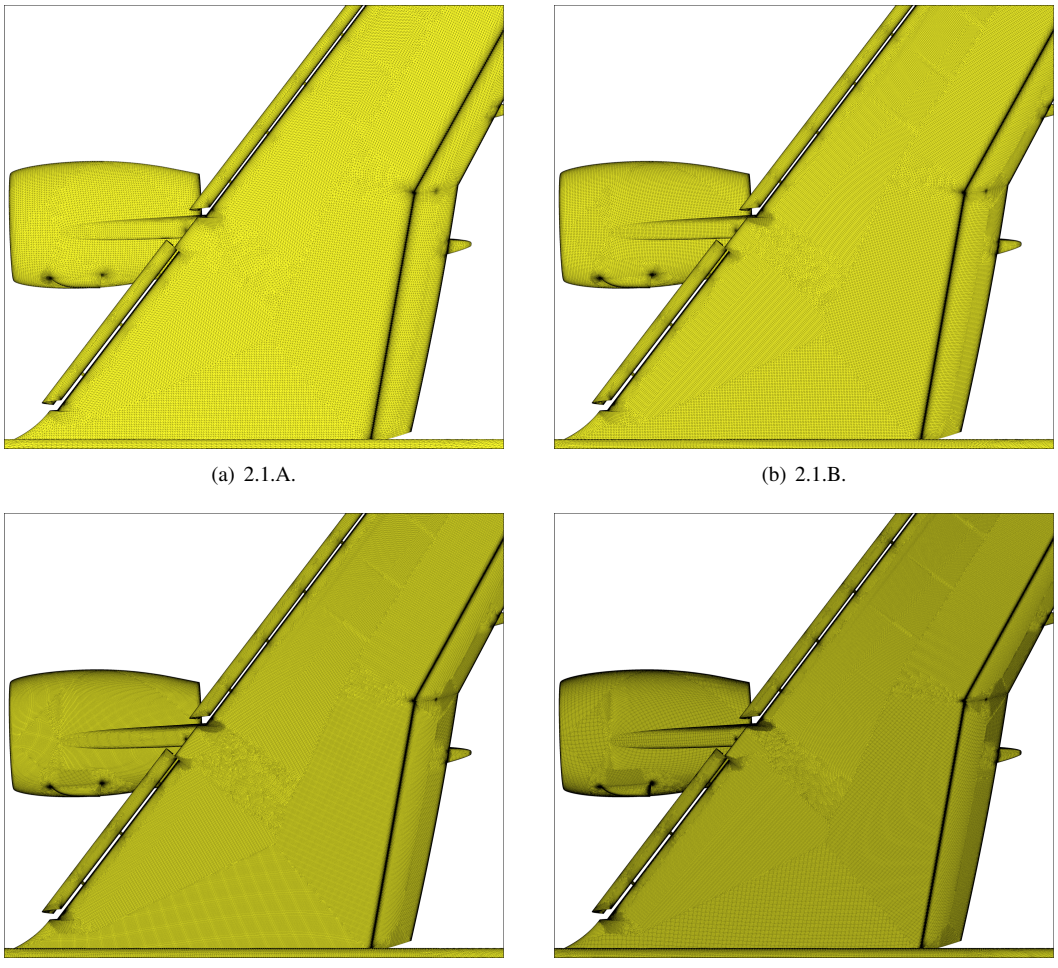

(a) 2.1.A. (b) 2.1.B.

(c) 2.1.C. (d) 2.1.D.

Fig. 3 Illustration of the Tetrahedral Grids for the CRM-HL Configuration (Nominal Flap Deflection).

Table 3 Tetrahedral Grid Sizes for CRM-HL Geometry.

Grid	Flap Deflection (inboard/outboard)	Cells (millions)	Nodes (millions)
2.1.A	40°/37°(nominal)	70.57	11.94
2.1.B	40°/37°(nominal)	188.12	31.66
2.1.C	40°/37°(nominal)	543.61	91.11
2.1.D	40°/37°(nominal)	1,211.01	202.55
2.1.37/34.D	37°/34°	1,197.20	200.23
2.1.43/40.D	43°/40°	1,194.69	199.81

The grids for the 2DMEA geometry are available for download at the TMR website [30]. Similar to 3D CRM-HL geometry, multiple sets of grids are available including two unstructured grid families (Family 1 and 2) and one structured, overset grid family (Family 3). However, only Family 1 was available at the time the analysis was performed. Family 1 consists of seven grid levels with approximately a factor of two increase in the number of nodes between two successive grids. The grids feature both prism and hexahedral element types and have a span of one grid unit to enable simulation using three-dimensional solvers. An illustration of the L1 (coarsest), L3, L5, and L7 (finest) grids is provided in Figure 4 and the grid sizes are provided in Table 4.

Table 4 Famliy 1, Mixed-Element Grid Sizes for 2DMEA Geometry.

Grid	Cells (millions)	Nodes (millions)
L1	0.174	0.348
L2	0.295	0.588
L3	0.508	1.016
L4	0.931	1.861
L5	1.680	3.360
L6	3.228	6.456
L7	5.981	11.961

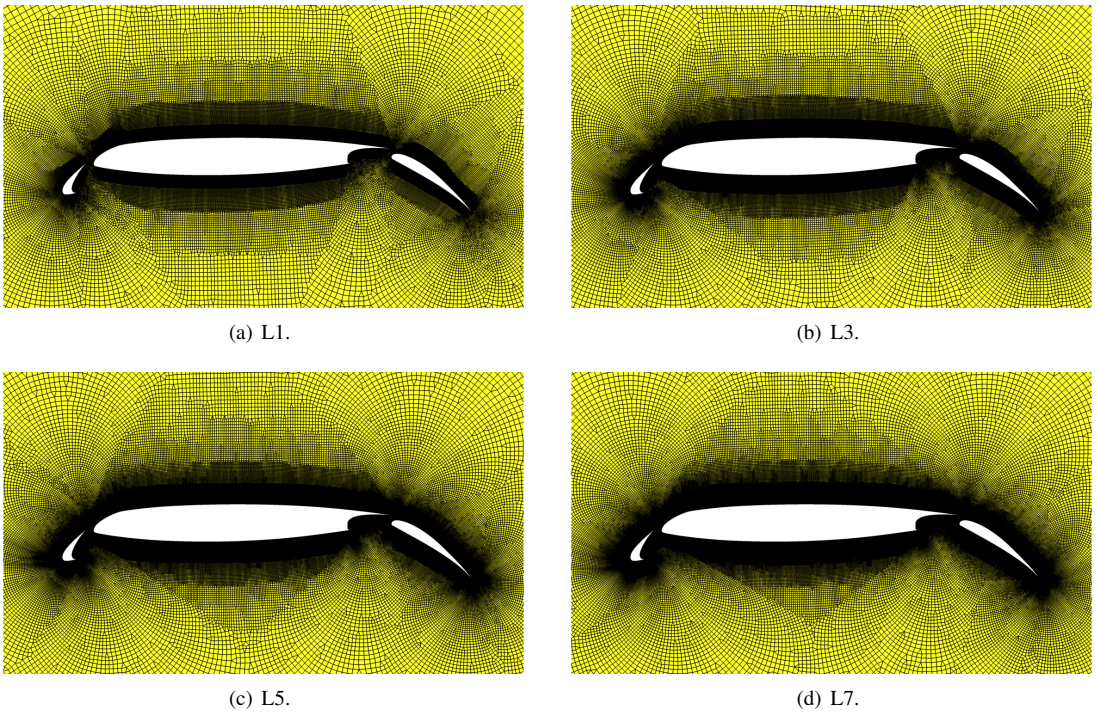

(a) L1. (b) L3.

(c) L5. (d) L7.

Fig. 4 Illustration of the Family 1, Mixed-Element Grids for 2DMEA Geometry.

E. Test Cases

The workshop participants were asked to perform simulations for three test cases. Case 1 was subdivided into two parts; Case 1a consisted of investigating the impact of flap deflection angle for the finest grid available and Case 1b consisted of performing a grid refinement study at the nominal flap settings. Note that Case 1b was given as an optional test case. Case 2 consisted of performing angle-of-attack sweeps for the nominal flap deflection to investigate the ability

to predict $C_{L,max}$ and was also subdivided into two parts; Case 2a consisted of a pitch sweep using the wall-corrected angles of attack in free-air and Case 2b was a repeat of Case 2a, but with the uncorrected angles of attack and including the tunnel walls. Case 2b was also optional. Case 3 consisted of performing a turbulence model verification study using a 2D slice of the CRM-HL wing. This case consisted of performing simulations using the grid family provided on the TMR website [30] and comparing the predicted quantities to those provided. For this work, Cases 1a, 1b, 2a, and 3 were computed. A summary of the described test cases are provided in Tables 5 through 7 below.

Table 5 Test Case 1.

	Case 1a	Case 1b
Geometry	CRM-HL	CRM-HL
Flap Deflection (inboard/outboard)	37°/34°, 40°/37°(nominal), 43°/40°	40°/37°(nominal)
Slat Deflection (inboard/outboard)	30°/30°	30°/30°
Grid(s)	2.1.37/34.D, 2.1.D, 2.1.43/40.D	2.1.A, 2.1.B, 2.1.C, 2.1.D
Mach	0.2	0.2
Re_{MAC} (millions)	5.49	5.49
Angle(s) of Attack (wall corrected)	7.05°	7.05°

Table 6 Test Case 2.

	Case 2a
Geometry	CRM-HL
Flap Deflection (inboard/outboard)	40°/37°(nominal)
Slat Deflection (inboard/outboard)	30°/30°
Grid(s)	2.1.D
Mach	0.2
Re_{MAC} (millions)	5.49
Angle(s) of Attack (wall corrected)	2.78°, 7.05°, 11.29°, 17.05°, 19.57°, 20.55°, 21.47°

Table 7 Test Case 3.

	Case 3
Geometry	2D Multielement Airfoil
Flap Deflection	37°
Slat Deflection	30°
Grid(s)	Family 1, Mixed-Element
Mach	0.2
Re_{MAC} (millions)	5.0
Angle(s) of Attack	16.0°

IV. Results

The results of the USM3D-ME simulations performed for HLPW4 are discussed in this section. Sections IV.A and IV.B provide results and discussion for the flap deflection and grid refinement studies. Similarly, the results and discussion for the angle-of-attack sweep and turbulence model studies for the nominal flap deflection configuration are provided in Section IV.C. Finally, Section IV.D describes the results of the turbulence model verification exercise performed for the 2DMEA geometry.

A. Case 1a: Flap Deflection Study

As described in Table 5, the finest grid refinement level was used for the flap deflection study, which considered three total configurations. Additionally, all Case 1 simulations were performed at 7.05° angle of attack. The convergence history and force and moment coefficient results are provided in this subsection including comparisons with the experimental data.

1. Convergence

The iterative convergence histories for the three flap deflection cases are provided in Figure 5. Figure 5a illustrates the combined mean flow and turbulence residual histories, which shows 4.5 to 5 orders of magnitude reduction before the residuals reach a limit cycle. Ideally, the residuals should be reduced to machine zero. However, that was not achieved for the cases shown here. The lift coefficient histories provided in Figure 5b show that the lift coefficient does converge for all cases. Note that the described simulations required more than 100,000 HANIM iterations to achieve converged forces and moments for some cases.

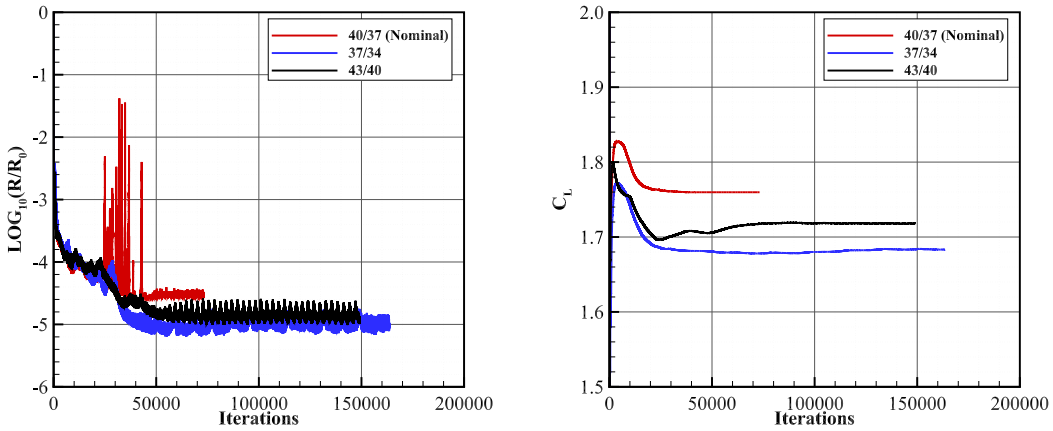

(a) Residual history.

(b) Lift coefficient, C_L, history.

Fig. 5 Iterative history for Case 1a.

2. Comparisons to Experimental Data

The resulting force and moment coefficients and lift-to-drag ratio are illustrated in Figure 6 along with the experimental data. Note that the data are plotted against the inboard flap angle. The corresponding outboard flap angle for each inboard flap angle can be found in Table 1. The results show that the computed results fail to accurately capture the trend observed in the experimental data. However, the USM3D-ME simulations are consistent with the submissions to the Fixed Grid for RANS TFG [6], which indicates that USM3D-ME is performing well when compared to HLPW4 participants with RANS methods. Differences between the RANS calculations and the wind tunnel measurements is assumed to be a limitation of RANS modeling for this application [5]. The results show that the USM3D-ME predictions for the nominal flap deflection (40° inboard flap deflection) agree better with the experimental data relative to the other two flap deflections. The largest differences are observed for the pitching moment coefficient, with observed differences as large as 10%.

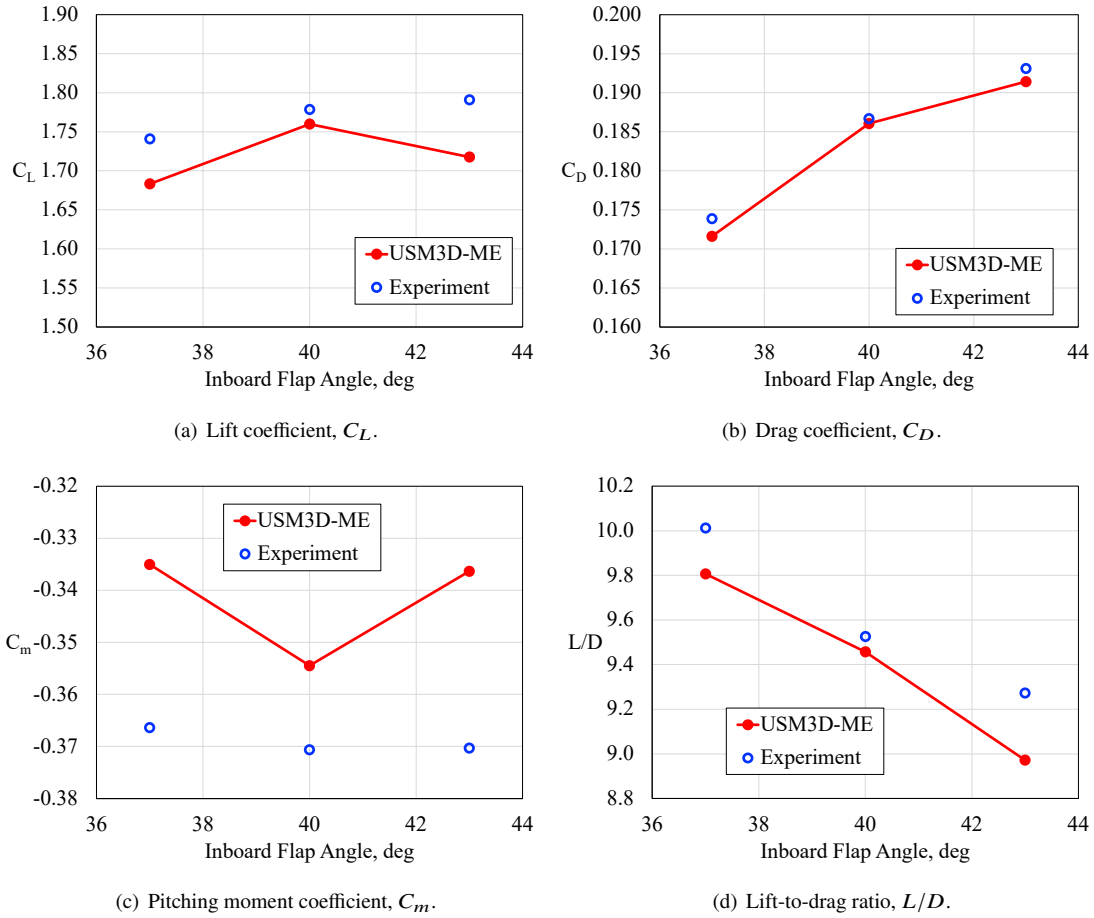

(a) Lift coefficient, C_L.

(b) Drag coefficient, C_D.

(c) Pitching moment coefficient, C_m.

(d) Lift-to-drag ratio, L/D.

Fig. 6 Force and moment coefficient comparisons for Case 1a.

B. Case 1b: Grid Refinement Study

The grid refinement study was performed for the nominal flap deflection at 7.05° angle of attack. Participants were instructed to perform simulations using the three finest grids that their computational resources would allow. For this work, all four grid refinements were simulated. Additionally, an adaptive-grid simulation was performed using the method described in Section III.B for comparison to the provided grids. The iterative histories and resulting force and moment coefficients are provided below.

1. Convergence

The iterative convergence histories for the four provided grid levels are provided in Figure 7. Similar to the behavior observed in Section IV.A, the combined residuals were reduced by 4-5 orders of magnitude. The lift coefficient histories show that convergence was achieved for all grids by 80,000 iterations.

The adaptive-grid simulation was performed for 62 adaptation cycles for a total of 620,000 flow iterations. The final grid size for the adapted grid was 321,047,626 cells. The iterative history for the final adapted grid is provided in Figure 8. The results in Figure 8 show that the flow residuals were reduced by 2.5 orders of magnitude before reaching a limit cycle behavior. Note that this case was started from a previous solution such that the starting residual values were smaller compared to previously discussed cases. The lift coefficient initially shows large oscillations, but settles down after around 4,000 iterations. After 4,000 iterations, the oscillations persist but are relatively small with a variation of roughly ± 0.05% around the mean value. Finally, an illustration of the final adapted grid is provided in Figure 9 along with the finest provided grid for comparison. The adapted grid features noticeably higher refinement in the slat and flap regions. Also, the region of the adapted grid downstream of the pylon exhibit cells that are aligned with the streamlines.

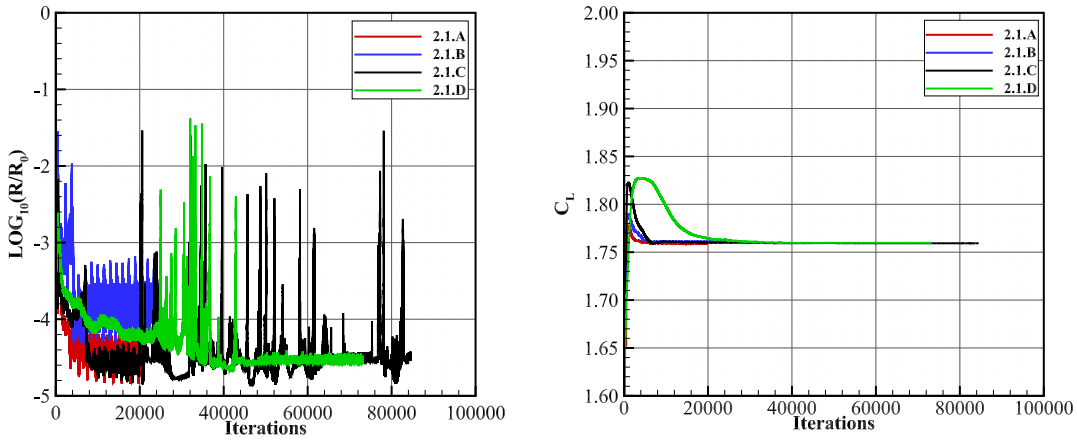

(a) Residual history.

(b) Lift coefficient, C_L, history.

Fig. 7 Iterative history for Case 1b, provided grids.

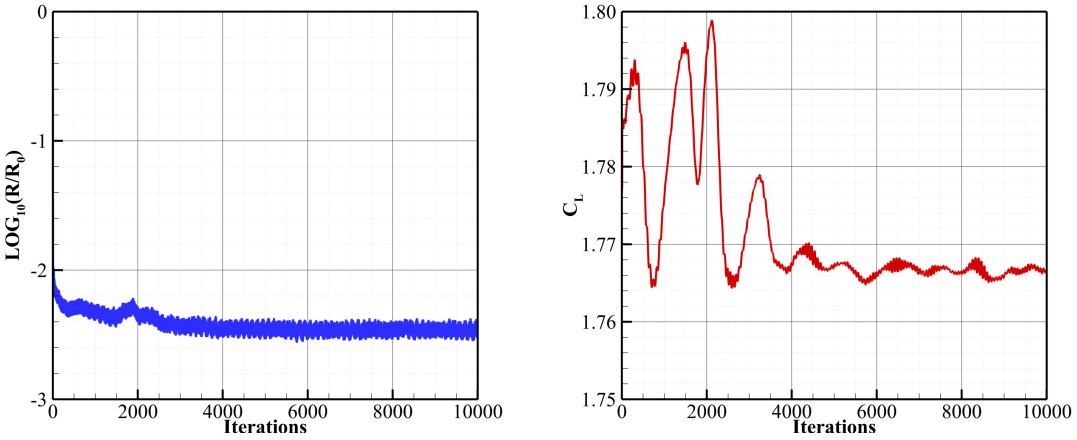

(a) Residual history.

(b) Lift coefficient, C_L, history.

Fig. 8 Iterative history for Case 1b, final adapted grid.

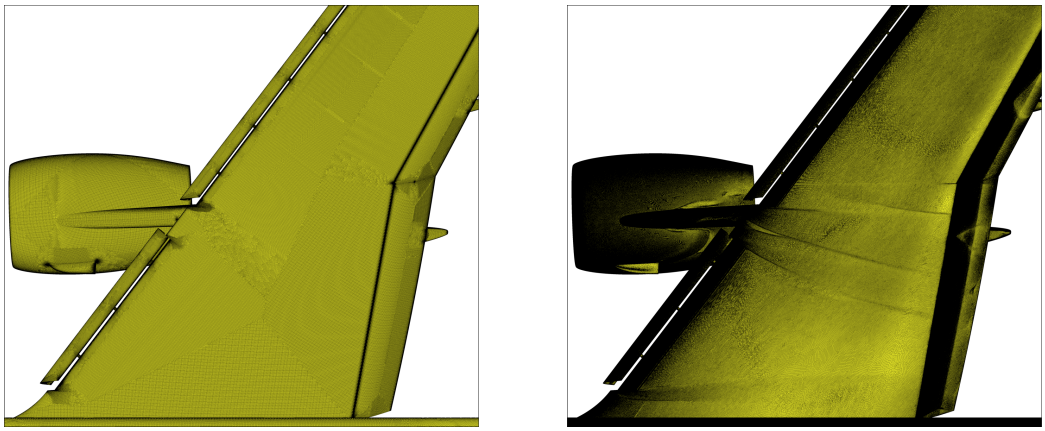

(a) Grid 2.1.D, 1,211.01×10^6 cells.

(b) Adapted Grid, 321.05×10^6 cells.

Fig. 9 Comparison of finest provided grid and the final adapted grid.

2. Comparisons to Experimental Data

The resulting force and moment coefficients for both the provided and adapted grids are plotted against grid size in Figure 10 with N denoting the number of cells in the grid. Additionally, the experimental values are included as dashed lines for reference. The results show that grid convergence was not achieved for any of the grids considered. The participants of HLPW4 struggled to demonstrate grid convergence for this configuration and flow condition [5]. Placing these results in the context of the Fixed Grid RANS TFG [6] and the Mesh Adaptation for RANS TFG [7] indicates that USM3D-ME is performing well as compared to peers. For the provided grids, the lift coefficient appears to be relatively converged, even for the coarsest grid level. However, the drag and pitching moment coefficients still exhibit relatively significant changes with grid refinement for the two finest grid levels. Additionally, the predicted pitching moment coefficient appears to be moving away from the experimentally measured value with increasing grid refinement with the provided grids. The adapted grids, on the other hand, appear to be approaching the experimental data with increasing refinement. However, further refinement is needed to evaluate whether this trend continues.

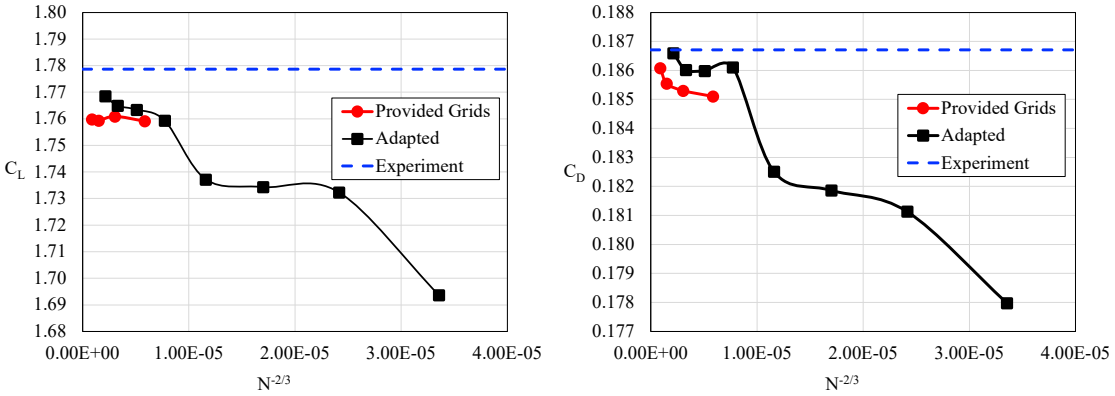

(a) Lift coefficient, C_L.

(b) Drag coefficient, C_D.

(c) Pitching moment coefficient, C_m.

Fig. 10 Force and moment coefficient comparisons for Case 1b.

3. Contour Plots and Comparisons to Oil Flow Images

HLPW4 participants were also provided with oil flow images for selected angles of attack that were produced during the wind tunnel test of the CRM-HL configuration. The oil flow images for the nominal flap deflection and 7.05° angle of attack are provided in Figure 11 for the upper surface of the wing.

The oil flow images in Figure 11 are divided into inboard and outboard portions. Note that the images correspond to a sideslip angle, β, of 5.99°, which corresponds to a wall-corrected angle of attack, α, of approximately 7.05°. Skin friction contour plots for both the provided grids and the adapted grid are provided in Figure 12 for comparison to the experimentally obtained oil flow images. The contour plots show qualitative agreement with experiment for all

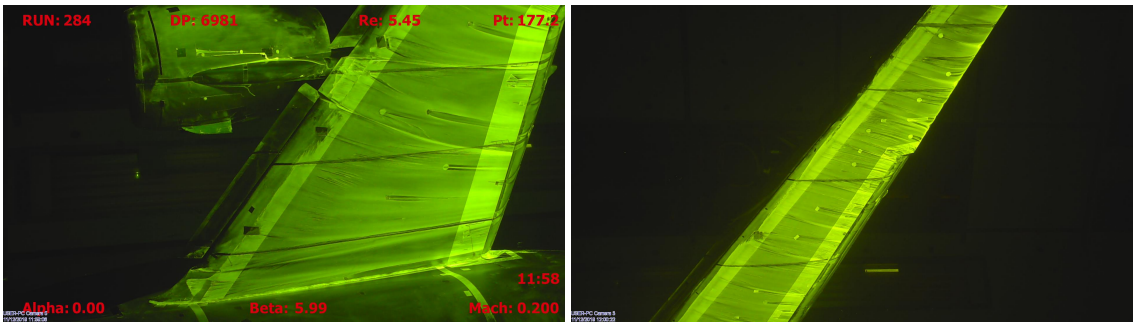

(a) Inboard. (b) Outboard.

Fig. 11 Oil flow images, upper surface, α = 7.05°.

grid levels, with the impact of grid refinement showing the greatest sensitivity in the pylon and outboard regions. Interestingly, the adapted grid solution, Figure 12e, appears to exhibit less resolution of the flow features near the root and midspan regions of the wing relative to the provided grids. However, this does not appear to negatively impact the integrated force and moment coefficient predictions shown in Figure 10 for the adapted grid.

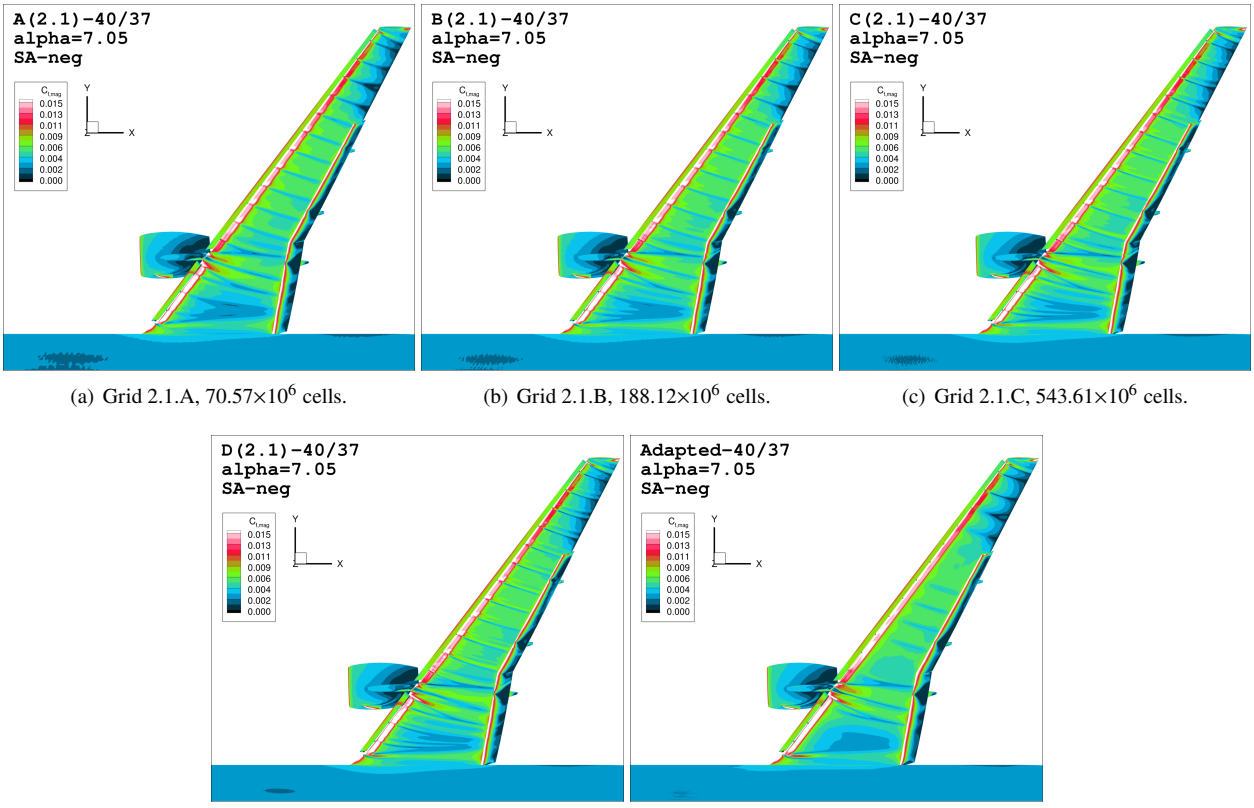

(a) Grid 2.1.A, 70.57×10^6 cells. (b) Grid 2.1.B, 188.12×10^6 cells. (c) Grid 2.1.C, 543.61×10^6 cells.

(d) Grid 2.1.D, 1,211.01×10^6 cells. (e) Adapted Grid, 321.05×10^6 cells.

Fig. 12 Contour plots of skin friction magnitude on upper surface, Case 1b.

4. Pressure Coefficient

Finally, the participants were provided with chordwise pressure coefficient data at eight spanwise stations along the wing. The station locations are illustrated in Figure 13. Figures 14 through 16 provide comparisons between the experiment and USM3D-ME for the slats, wing, and flaps and for both the provided grids and adapted grid.

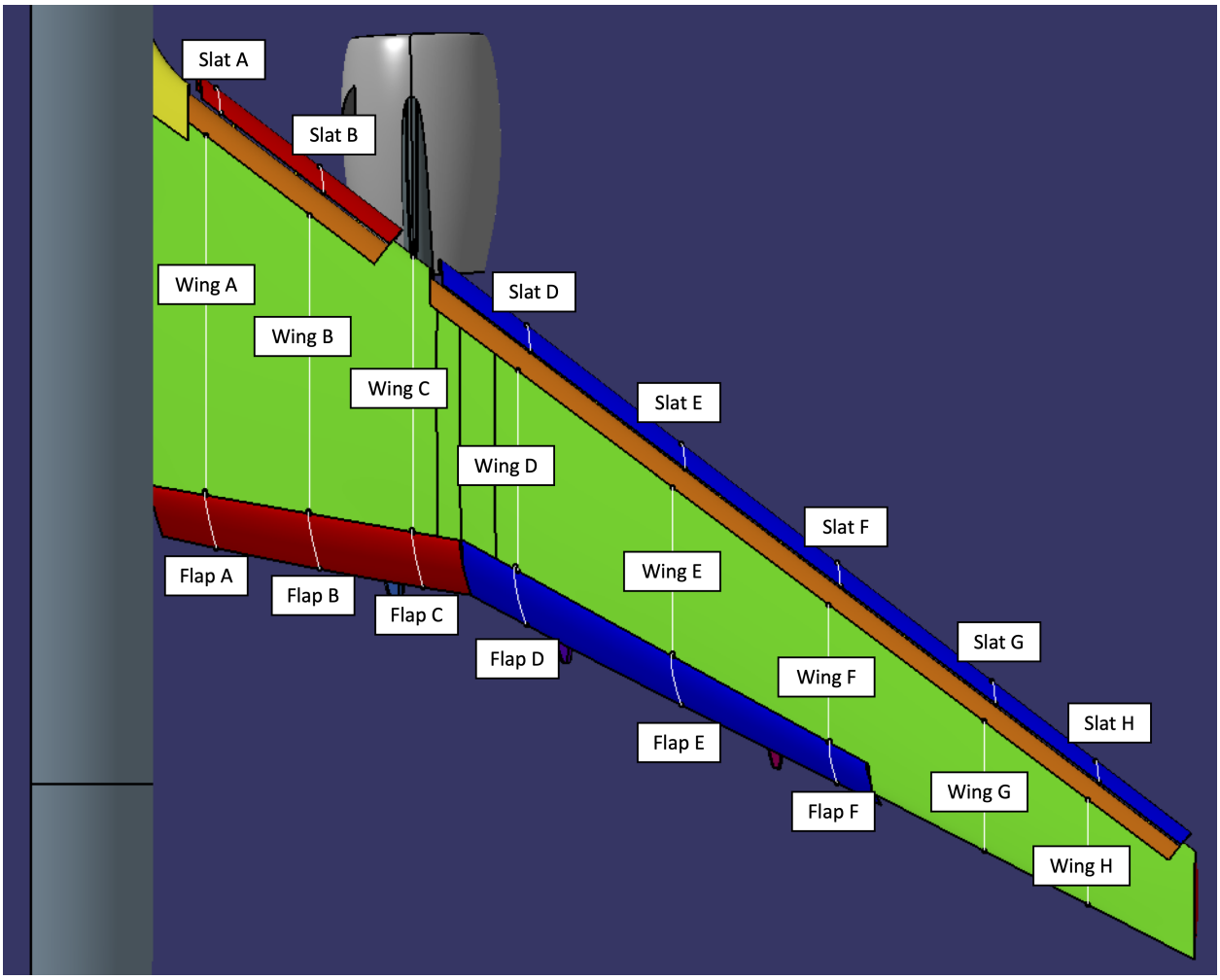

Fig. 13 Illustration of pressure tap stations.

The results show that both the greatest sensitivity to grid refinement and the largest differences between the USM3D-ME predictions and experiment occurs on the flaps. For the wing and slats, USM3D-ME shows a tendency to overpredict the pressure on the upper surface relative to the experimental data, with better general agreement observed on the lower surface. The differences observed for the flaps are the largest at the leading edge, where USM3D-ME underpredicts the suction peak. In general, although the pressure coefficient predictions do not show significant differences with increasing grid refinement, the adapted grid generally shows the best agreement with the experimental data.

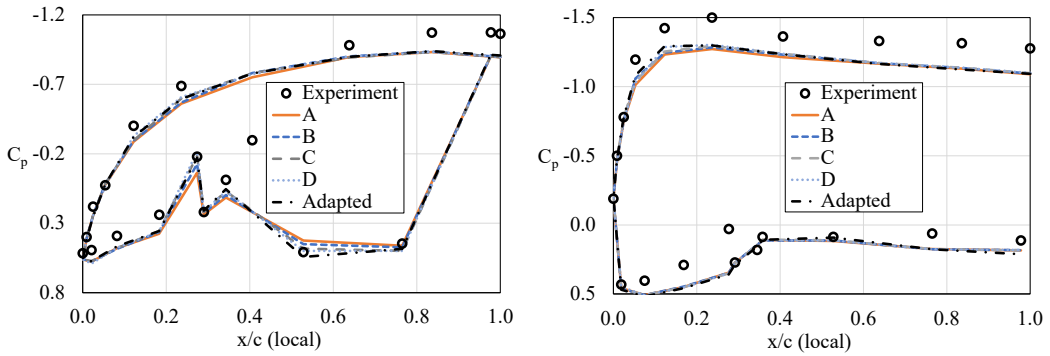

(a) Slat A.

(b) Slat B.

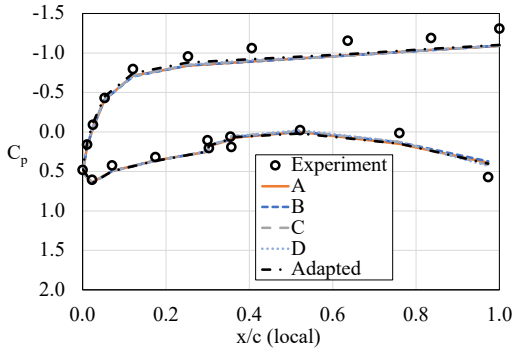

(c) Slat D.

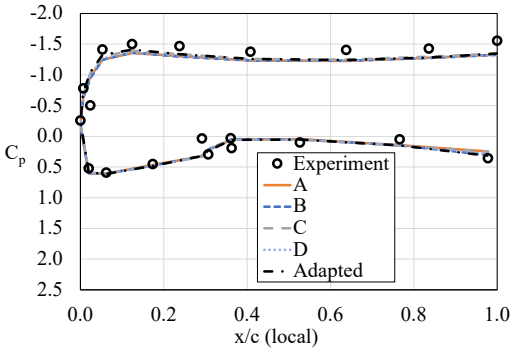

(d) Slat E.

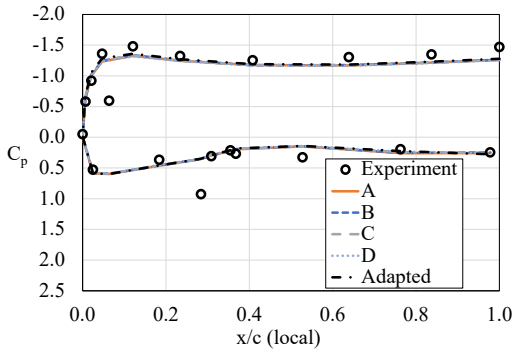

(e) Slat F.

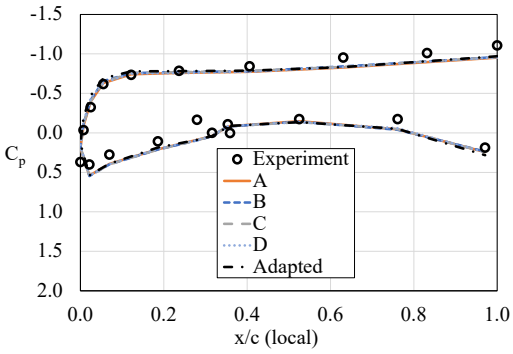

(f) Slat G.

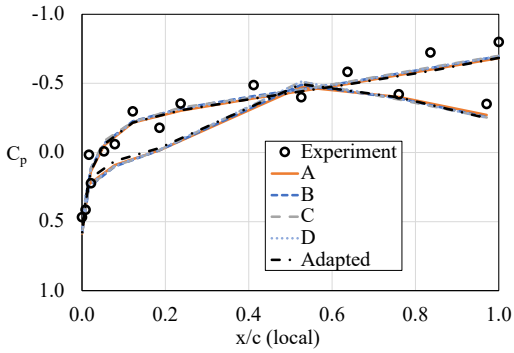

(g) Slat H.

Fig. 14 Pressure coefficient comparisons for slat, Case 1b.

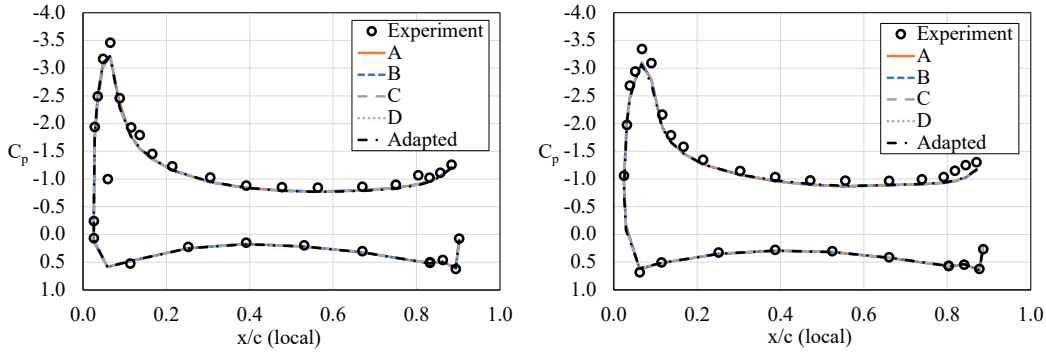

(a) Wing A.

(b) Wing B.

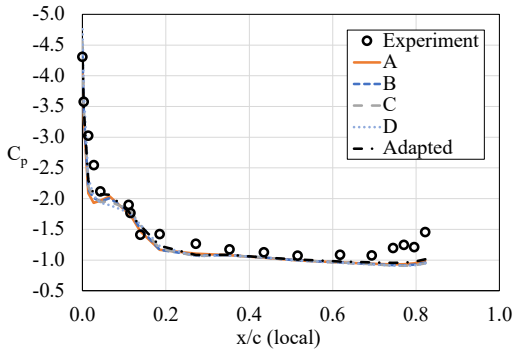

(c) Wing C.

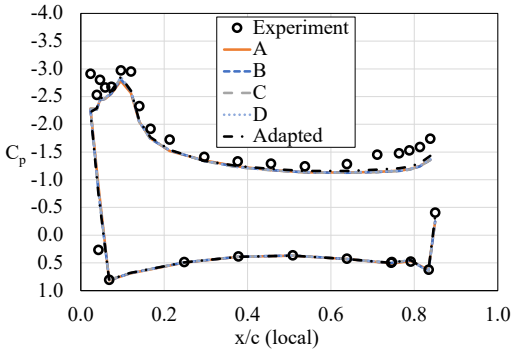

(d) Wing D.

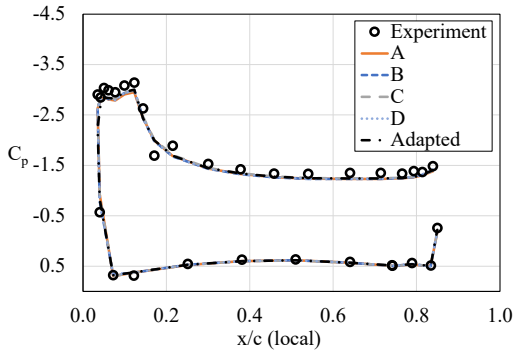

(e) Wing E.

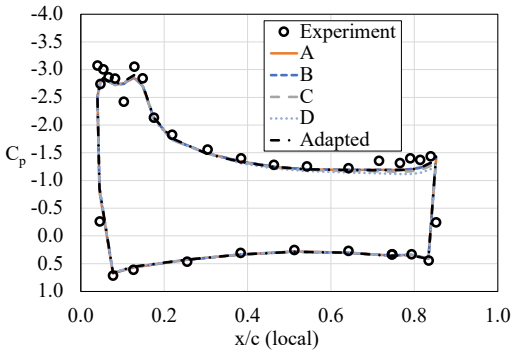

(f) Wing F.

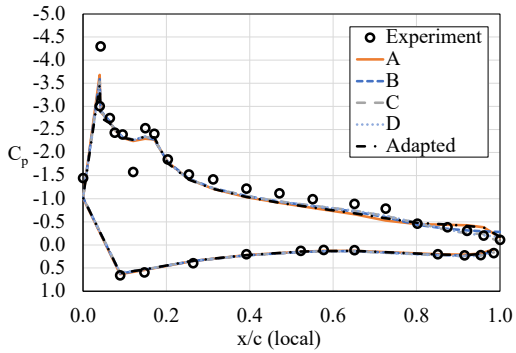

(g) Wing G.

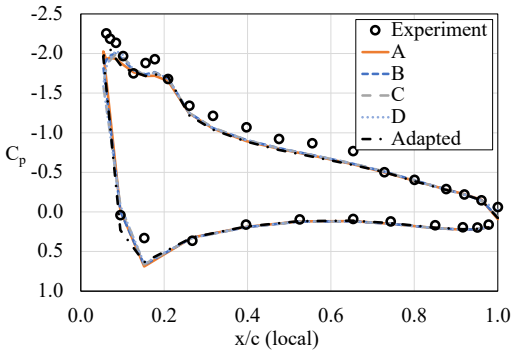

(h) Wing H.

Fig. 15 Pressure coefficient comparisons for wing, Case 1b.

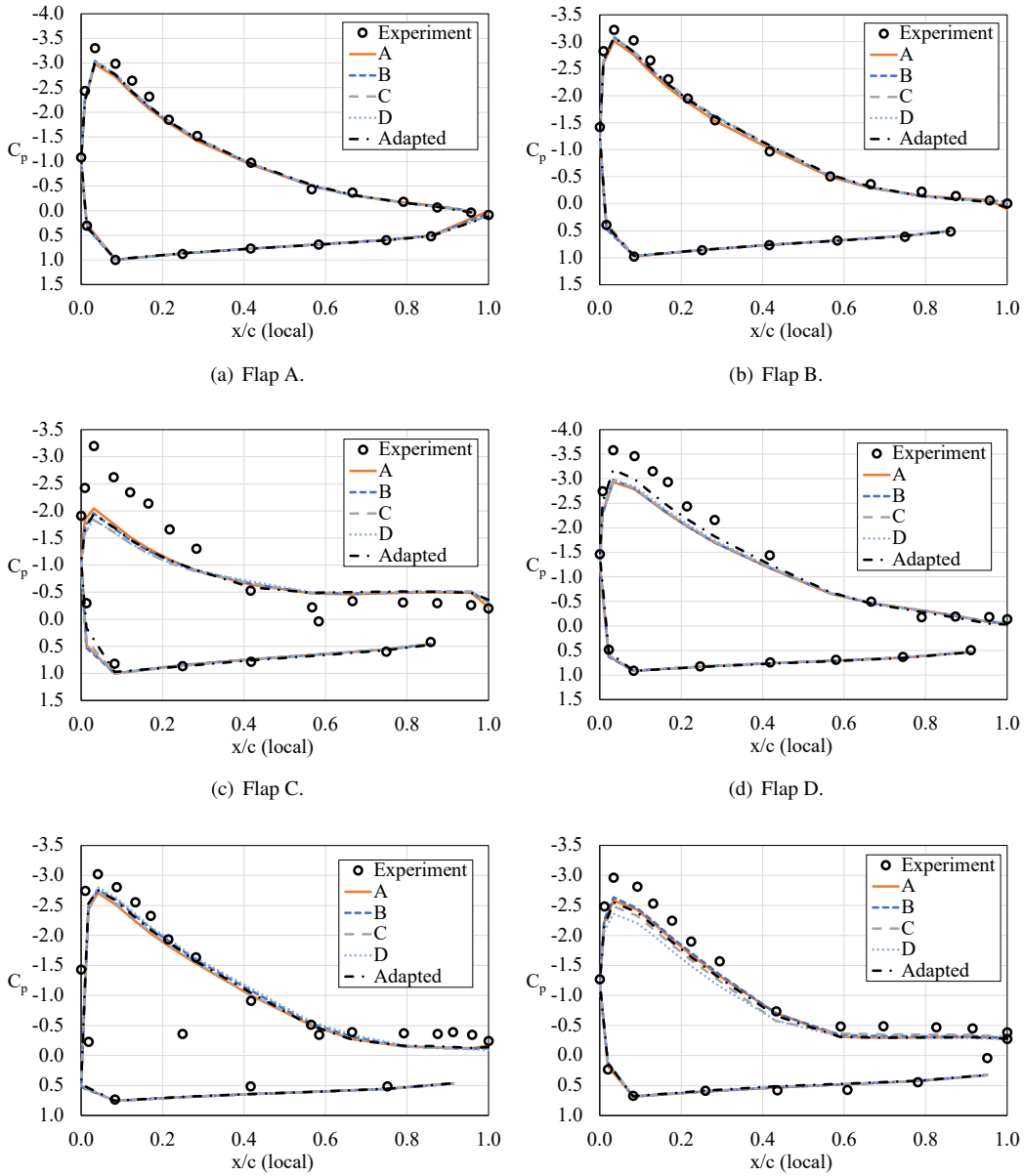

(a) Flap A.

(b) Flap B.

(c) Flap C.

(d) Flap D.

(e) Flap E.

(f) Flap F.

Fig. 16 Pressure coefficient comparisons for flap, Case 1b.

C. Case 2a: $C_{L,max}$ Study

For Case 2a, participants were asked to perform simulations of the CRM-HL for as many of the angle of attack values provided in Table 6 as possible. All simulations were performed for the finest provided grid level and the nominal flap deflection configuration. For this study, angle of attack values of 2.78°, 7.05°, 11.29°, and 17.05° were simulated. In addition to the baseline SA-neg turbulence model, the one-equation Spalart-Allmaras model with the rotation correction and the Quadratic Constitutive Relation (QCR-2000), denoted as SA-neg-RC-QCR, was employed to investigate the impact of turbulence model on the predicted force and moment coefficients. The iterative convergence histories and predicted force and moment coefficients are provided in this subsection. Note that since the angle-of-attack range was limited to 17.05° for this work, this is not technically a $C_{L,max}$ study. However, the data were submitted to the $C_{L,max}$ subtopic group for comparisons with other codes over a range of angles of attack.

1. Convergence

The residual histories provided for the computations based on the SA-neg model, shown in Figure 17a, are representative of the behavior observed for Case 1. Figure 17b provides the residual histories for the SA-neg-RC-QCR simulations, which were restarted from the baseline SA-neg solutions. The results show that the residuals histories for the SA-neg-RC-QCR simulations are similar in behavior to the SA-neg histories, but generally show less reduction in the residuals. The results provided in Figures 17c and 17d show that converged lift coefficients are achieved with both models considered.

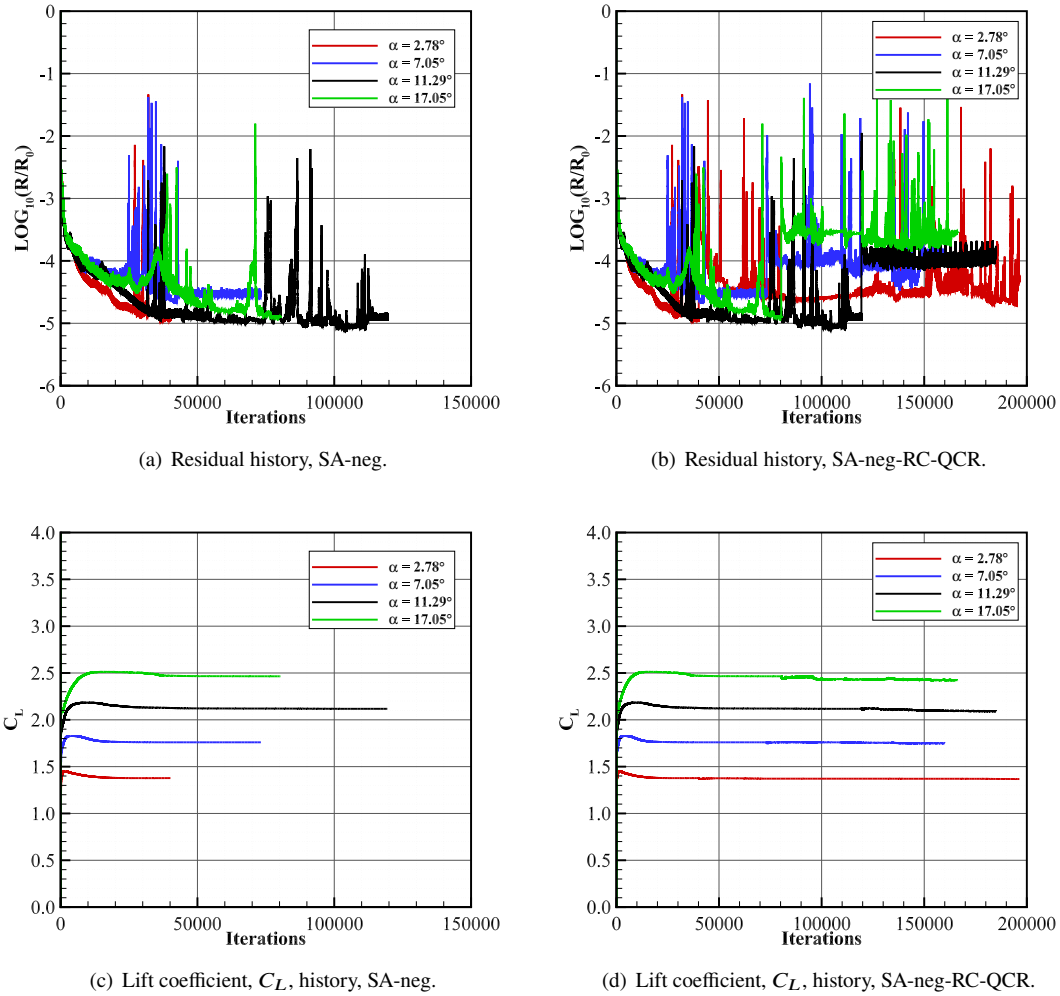

(a) Residual history, SA-neg.

(b) Residual history, SA-neg-RC-QCR.

(c) Lift coefficient, C_L, history, SA-neg.

(d) Lift coefficient, C_L, history, SA-neg-RC-QCR.

Fig. 17 Iterative history for Case 2a.

2. Comparisons to Experimental Data

The resulting force and moment coefficients are plotted against angle of attack in Figure 18 along with the provided experimental data. Additionally, the corresponding drag polars are provided for comparison.The results show that the SA-neg predictions, generally, agree better with the experimental data relative to the SA-neg-RC-QCR predictions. The predicted drag coefficients for the two models are in good agreement. However, the SA-neg-RC-QCR model exhibits a tendency to underpredict the lift coefficient and to predict a lower magnitude for pitching moment coefficient relative to the SA-neg model. The differences between the SA-neg and SA-neg-RC-QCR predictions are observed to increase with increasing angle of attack. These results are consistent with the Fixed Grid RANS TFG [6] submissions.

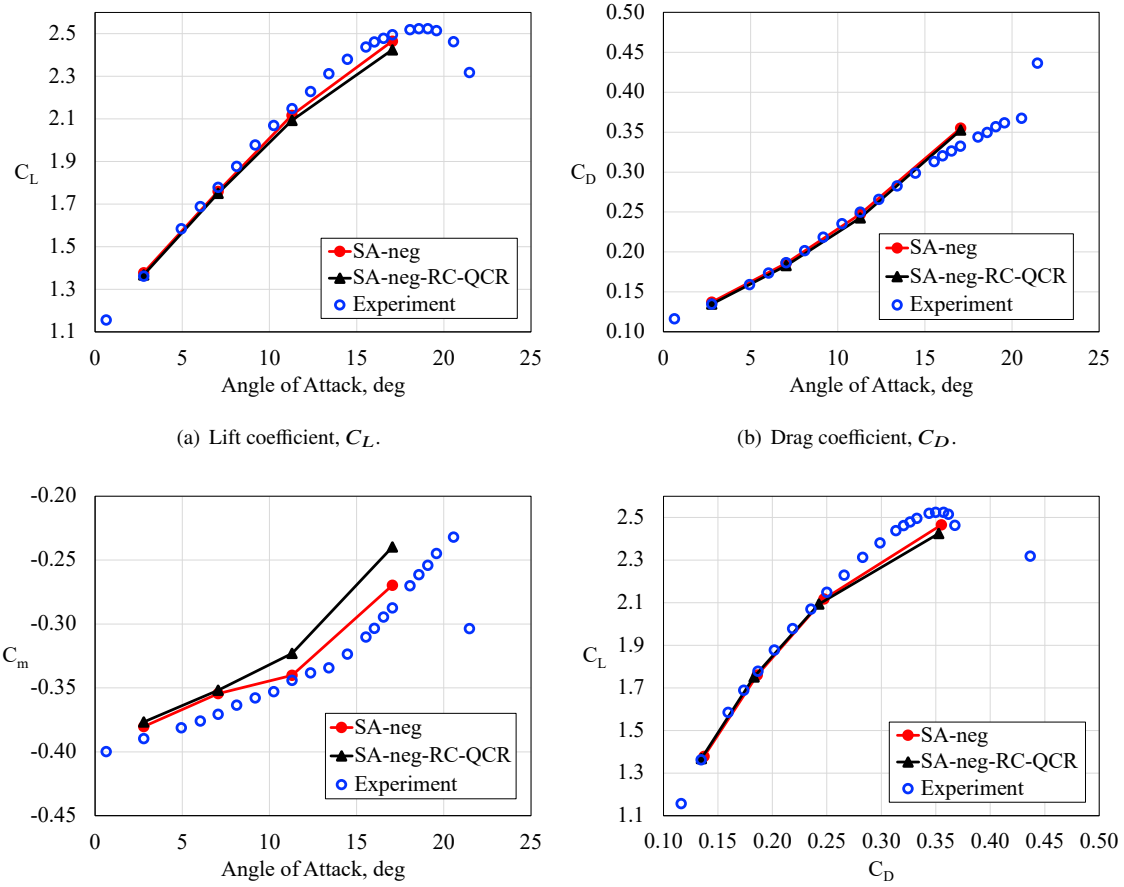

(a) Lift coefficient, C_L.

(b) Drag coefficient, C_D.

(c) Pitching moment coefficient, C_m.

(d) Drag polar.

Fig. 18 Force and moment coefficient comparisons for Case 2a.

3. Contour Plots

Among the four angles of attack considered here, the largest differences between the SA-neg and SA-neg-RC-QCR models was observed at 17.05°. To investigate these differences further, contour plots of the skin friction magnitude are shown in Figure 19. The contour plots show that the both models predict significant separation near the wing tip. The SA-neg-RC-QCR model exhibits the greatest extent of separation. Oil flow images from the experiment were not provided for this angle of attack. The outboard separation patterns are expected for RANS methods [5–7].

4. Pressure Coefficients for $\alpha = 17.05°$

Finally, the pressure cofficient predictions corresponding to the stations shown in Figure 13 are compared for both turbulence models and on the slat, wing, and flaps in Figures 20 through 22.

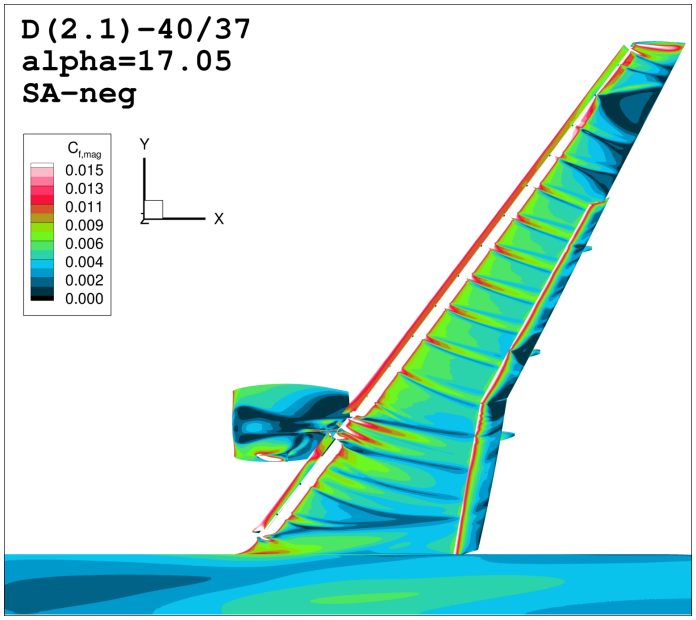

(a) SA-neg.

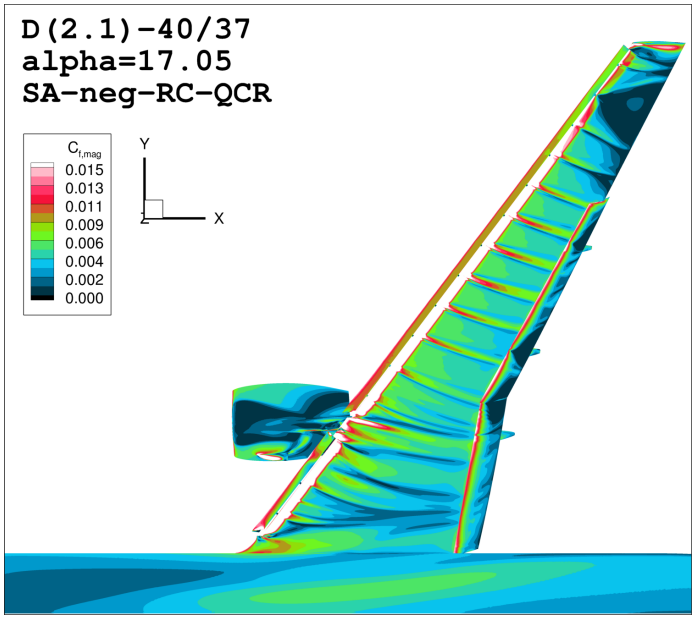

(b) SA-neg-RC-QCR.

Fig. 19 Contour plots of skin friction magnitude on upper surface, α = 17.05°, Grid 2.1.D, 1,211.01×10^6 cells.

The pressure coefficient comparisons show small differences between the SA-neg and SA-neg-RC-QCR predictions for the slats and wing stations. Both models agree favorably with the experimental data with the exception of the most outboard cross-section (station H), where both models predict higher pressure on the upper surface relative to the experiment. The largest difference occurs for the wing at Station H where USM3D drastically underpredicts the suction peak. For the flaps, there are more discernable differences in the pressure coefficients predicted by the two turbulence models. It is not clear whether one model is superior, with the SA-neg model matching the experimental data better for some stations and the SA-neg-RC-QCR model matching better for others. However, both models show a general tendency to underpredict the suction peak on the flaps.

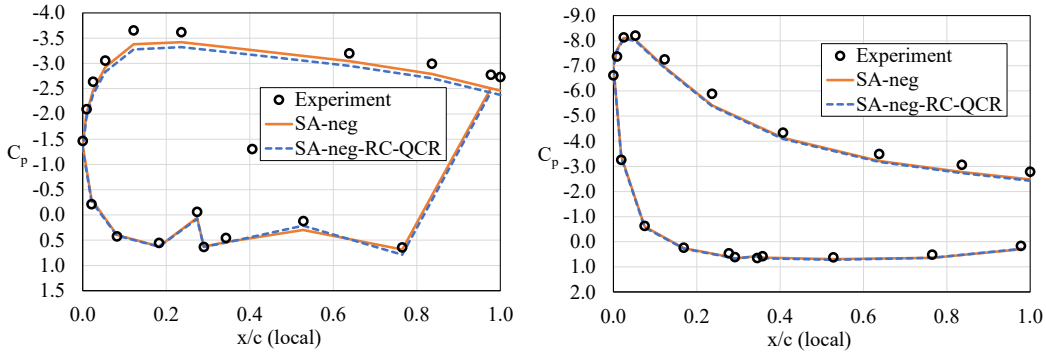

(a) Slat A.

(b) Slat B.

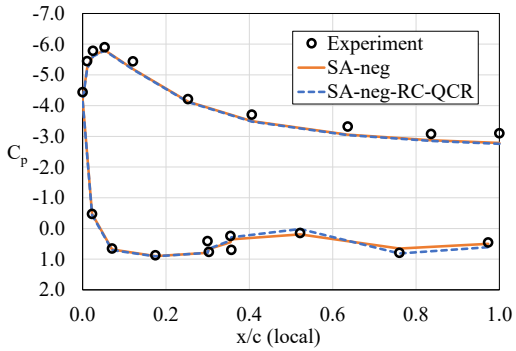

(c) Slat D.

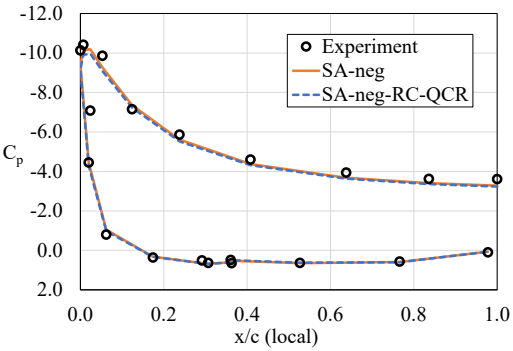

(d) Slat E.

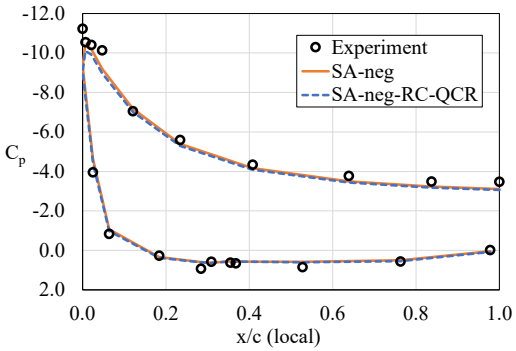

(e) Slat F.

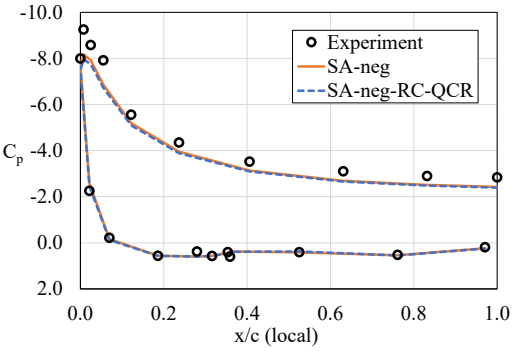

(f) Slat G.

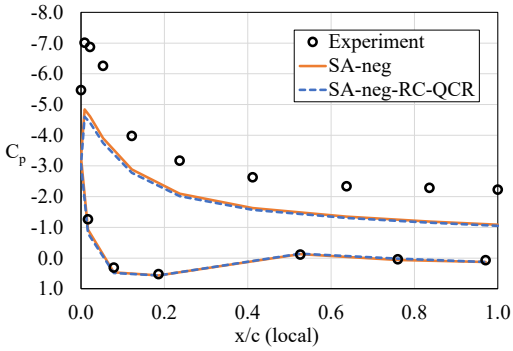

(g) Slat H.

Fig. 20 Pressure coefficient comparisons for slat, α = 17.05°.

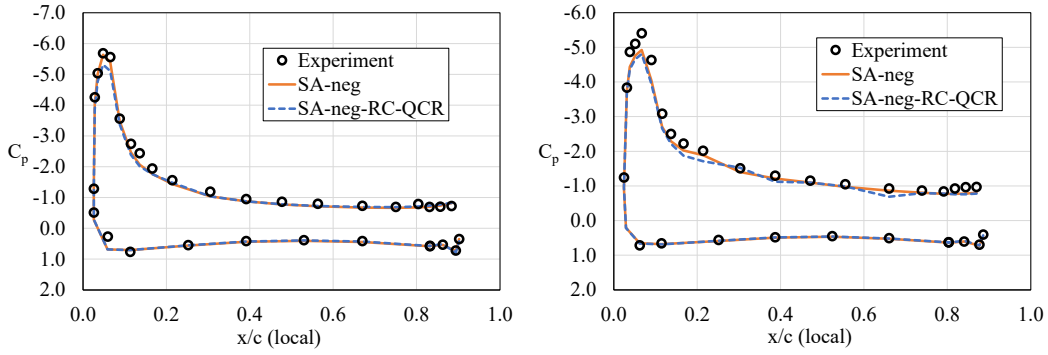

(a) Wing A. (b) Wing B.

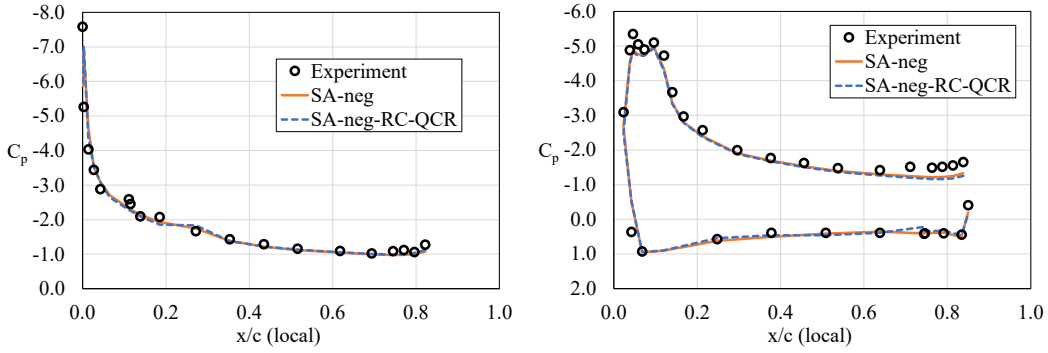

(c) Wing C. (d) Wing D.

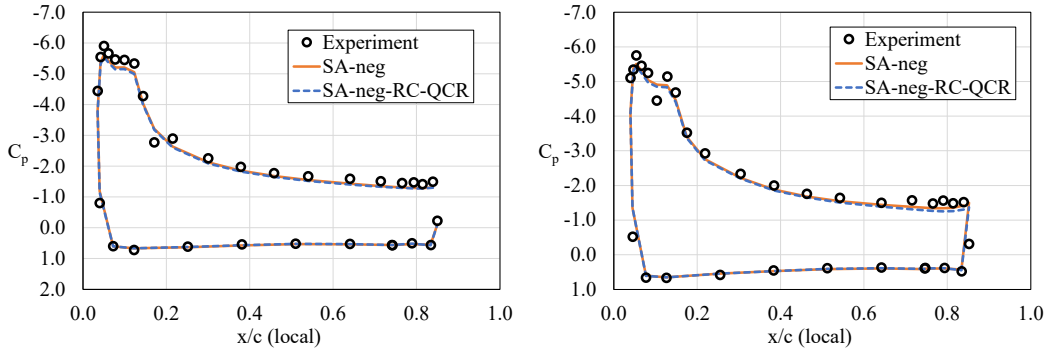

(e) Wing E. (f) Wing F.

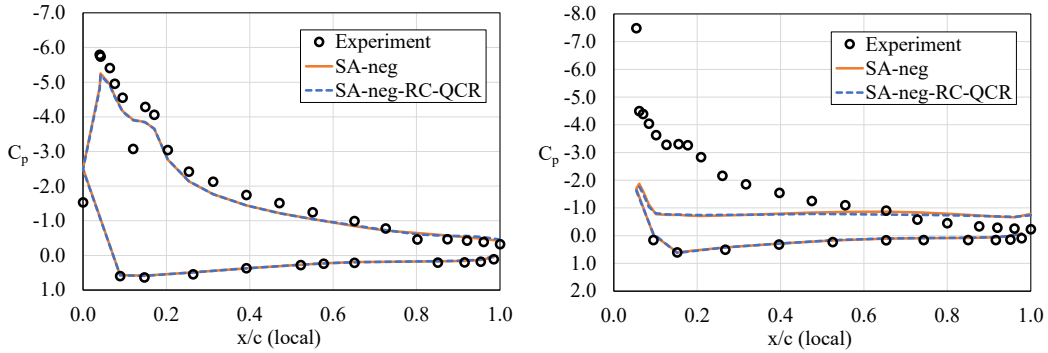

(g) Wing G. (h) Wing H.

Fig. 21 Pressure coefficient comparisons for wing, α = 17.05°.

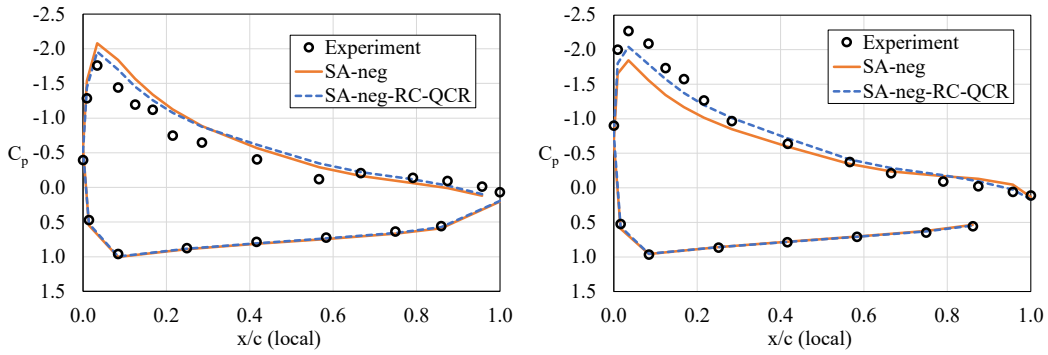

(a) Flap A.

(b) Flap B.

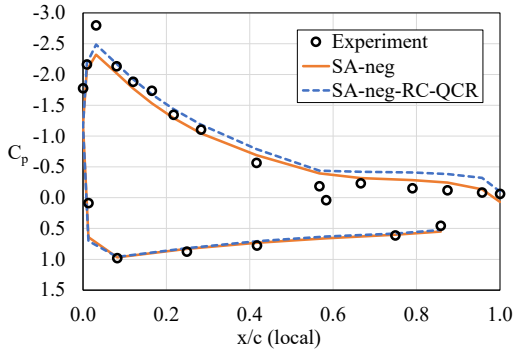

(c) Flap C.

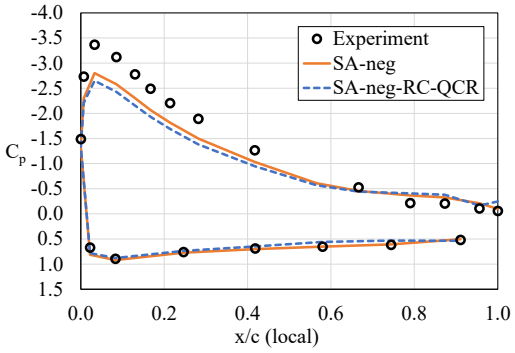

(d) Flap D.

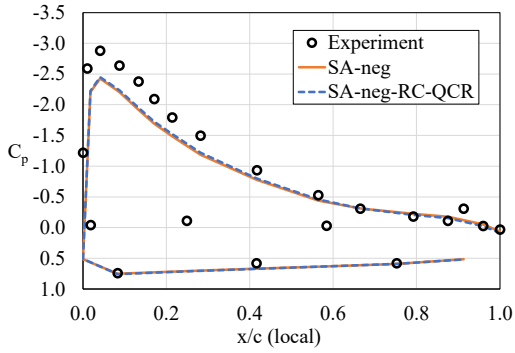

(e) Flap E.

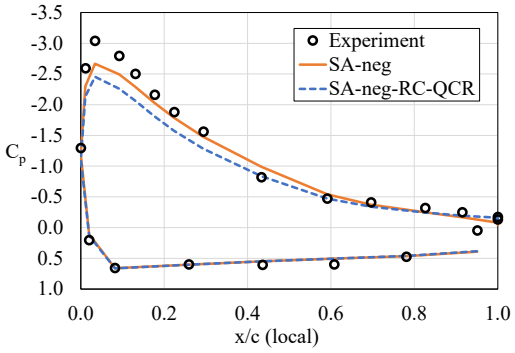

(f) Flap F.

Fig. 22 Pressure coefficient comparisons for flap, α = 17.05°.

D. Case 3: Turbulence Model Verification Study

The final study discussed in this section is the turbulence model verification study. Note that this study was performed prior to Cases 1 and 2. The iterative histories and predicted force and moment coefficients for the 2DMEA configuration are provided in the following subsections.

1. Convergence

The iterative histories of the residuals and lift coefficient are provided in Figure 23 for the seven grid refinements (Family 1 on the TMR website [30]). The results show that grids L4-L7 are converged approximately ten orders of magnitude after 5,000 iterations or less. Grids L1-L3 required more than 40,000 iterations to converge and exhibited roughly 8 orders of magnitude reduction in residuals. Note that grids L1-L3 exhibited convergence issues that required significant restrictions to the maximum CFL enforced by HANIM and took longer to converge as a result. However, the lift coefficient histories show that all grids were converged by 20,000 iterations.

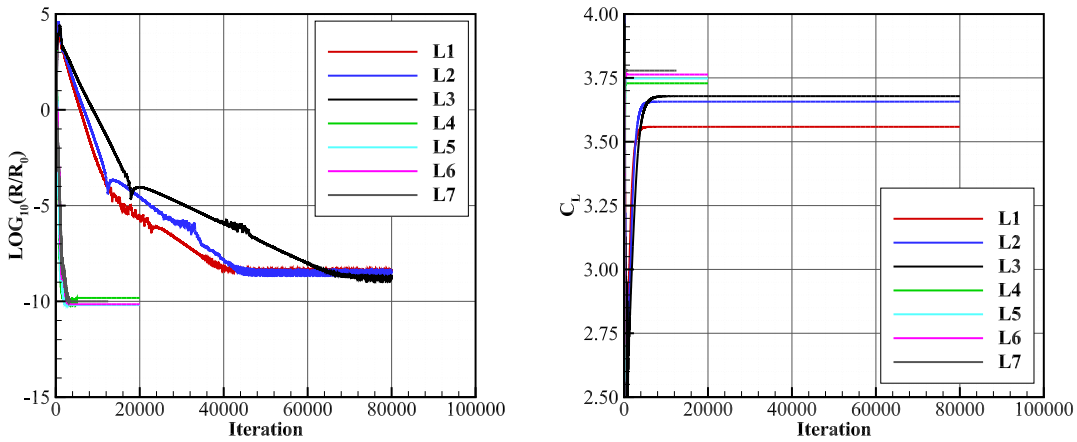

(a) Residual history.

(b) Lift coefficient, C_L, history.

Fig. 23 Iterative history for Case 3.

2. Comparisons to other Predictions

The resulting force and moment coefficients are plotted against grid size, N, in Figure 24. The plots also include predictions from a variety of other flow solvers that are available on the TMR website [30]. Note that FUN3D and USM3D-ME predictions are provided for the both the fixed grids discussed in Section III.D and for solution-adaptive grids for comparison. The results show that the USM3D-ME and FUN3D predictions agree favorably. Although neither solver achieved grid convergence for the fixed grid solutions, the predicted force and moment coefficients trend towards the adapted grid solutions with increasing grid refinement. The adapted grid predictions for FUN3D and USM3D-ME illustrate converged force and moment coefficients that compare favorably with those provided by the other codes. These results indicate a consistent implementation of the SA-neg model in the USM3D-ME solver and provide confidence for the CRM-HL simulations that followed.

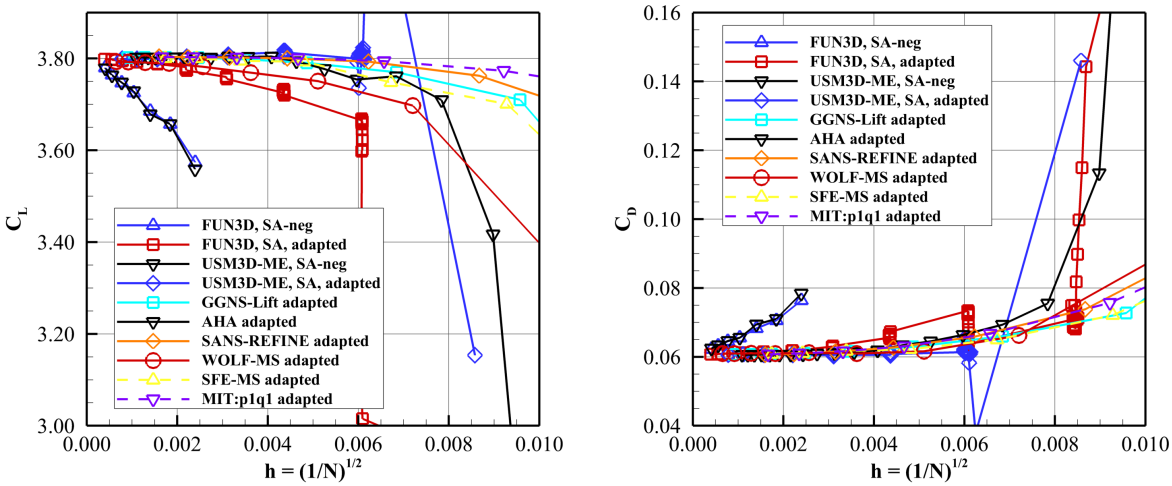

(a) Lift coefficient, C_L.

(b) Drag coefficient, C_D.

(c) Pitching moment coefficient, C_m.

Fig. 24 Force and moment coefficient comparisons for Case 3.

V. Summary and Conclusions

The 4th High-Lift Prediction Workshop (HLPW4) was held at the 2022 AIAA SciTech conference. This paper discusses the results of USM3D-ME simulations performed for HLPW4. Simulations were performed to predict the effects of flap deflection, grid refinement, and an angle-of-attack sweep on the computed force and moment coefficients as well as the flowfield. Additionally, the angle-of-attack sweep was performed using both SA-neg and SA-neg-RC-QCR models to investigate the impact of turbulence closure methods. The flap deflection results show that USM3D-ME tends to underpredict both the lift and drag coefficients, while predicting a less negative pitching moment coefficient relative to the experimental data. Additionally, the predictions for the nominal flap deflection case show better agreement with experiment than observed for the two off-nominal configurations. The grid refinement study showed that grid convergence was not achieved for the provided grids.

To investigate this further, a solution-adaptive grid simulation was performed for the nominal flap deflection at 7.05°angle of attack. The results showed that the solution-adaptive grid predictions trend towards the experimental data, but additional grid refinement would be needed to evaluate whether that trend continues. Consistent with the findings of the ADAPT TFG, the adapted grid prediction agreed better with the experimental data relative to the provided grids [32]. However, the adapted grid solutions also undepredicted the lift and drag coefficients and predicted a less negative

pitching moment coefficient relative to the experimental data.

Examining the pressure coefficient predictions at various spanwise stations, USM3D-ME generally compares well with the experimental data on the lower surfaces and overpredicts the pressure on the upper surface, with the largest differences observed on the flaps. The final case for the CRM-HL configuration consisted of performing an angle-of-attack sweep using both the SA-neg and SA-neg-RC-QCR turbulence models. The results show that both models tend to underpredict the lift coefficient and overpredict the drag coefficient with increasing angle of attack. Also, USM3D-ME predicted a less negative pitching moment coefficient for both turbulence models and all angles of attack. However, the SA-neg predictions agree more favorably with the experimental data relative to the SA-neg-RC-QCR turbulence model.

Finally, the turbulence model verification study was discussed, which was performed prior to the CRM-HL simulations. This study considered a grid family for the 2DMEA geometry, available for download on the TMR website [30]. The results showed that the USM3D-ME predictions agree favorably with the FUN3D predictions using the same grid family and trend towards the adapted grid solutions with increasing grid refinement.

An interesting observation from this work was the general lack of sensitivity to grid refinement for the RANS predictions performed using the provided grids. For the adapted grids, significant changes were observed in the predicted force and moment coefficients as the grid was progressively refined. This finding implies that the coarsest grid of the provided grids was already refined to the point of diminishing returns and further refinement did not provide significant benefit. Another unexpected finding for the USM3D-ME predictions was apparent from the turbulence modeling study, which showed the SA-neg predictions to agree better with the experimental data than observed for the SA-neg-RC-QCR predictions. This was an interesting result since both RC and QCR are generally considered a best practice for force and moment predictions. Overall, the USM3D-ME predictions discussed in this work were found to be in good general agreement with RANS predictions submitted by other participants employing various solvers.

One of the significant challenges associated with comparing CFD predictions to experimental data is matching the conditions between the two methods. For the HLPW4 workshop, the participants were asked to perform freeair simulations at fixed angles of attack that correspond to wall-corrected values from the experiment. In general, it is difficult to match the lift between the CFD and experiment due to a variety of factors such as wall effects, discretization error in the CFD, and model deformation in the experiment. Future work will extend the efforts discussed in this paper to include lift-matched CFD solutions, where the angle of attack in the CFD simulations will be varied to match the lift measured in the experiment. These solutions will then be employed for comparison to the experimentally obtained drag polar, pressure coefficient distributions, and oil flow images, which will provide more insight into the cause of some of the differences observed for this work. This will be discussed in a future paper.

Acknowledgements

This effort has been supported by the Commercial Supersonic Technology (CST) project. Special thanks are given to Nash'at Ahmad of NASA Langley for providing insight and discussion for this work. The authors would also like to thank the organizers of HLPW4 for providing this opportunity. Finally, acknowledgements are extended to the NASA Advanced Supercomputing (NAS) facility for providing the resources needed to perform this work. This work was partially supported by the Transformational Tools and Technologies (TTT) Project of the NASA Transformative Aeronautics Concepts Program (TACP) under the Aeronautics Research Mission Directorate.

References

[1] Rumsey, C. L., and Ying, S. X., "Prediction of High Lift: Review of Present CFD Capability," *Progress in Aerospace Sciences*, Vol. 38, No. 2, 2002, pp. 145–180.

[2] Rumsey, C. L., Slotnick, J. P., and Sclafani, A. J., "Overview and Summary of the Third AIAA High Lift Prediction Workshop," *Journal of Aircraft*, Vol. 56, No. 2, 2019, pp. 621–644.

[3] Lacy, D. S., and Clark, A. M., "Definition of Initial Landing and Takeoff Reference Configurations for the High Lift Common Research Model (CRM-HL)," *AIAA AVIATION 2020 FORUM*, 2020, p. 2771.

[4] Evans, A., Lacy, D., Smith, I., and Rivers, M., "Test Summary of the NASA Semi-Span High-Lift Common Research Model at the QinetiQ 5-Metre Low-Speed Wind Tunnel," AIAA Paper 2020–2770, 2020. doi:10.2514/6.2020-2770.

[5] Rumsey, C. L., Slotnick, J. P., and Woeber, C. D., "HLPW-4/GMGW-3: Overview and Workshop Summary," AIAA Paper 2022–3295, 2022. doi:10.2514/6.2022-3295.

[6] Ollivier-Gooch, C. F., and Coder, J. G., "Lessons Learned by the Fixed-Grid RANS TFG for HLPW-4 / GMGW-3," AIAA Paper 2022–3211, 2022. doi:10.2514/6.2022-3211.

[7] Park, M. A., Alauzet, F., and Michal, T., "HLPW-4/GMGW-3: Mesh Adaptation for RANS Technology Focus Group Workshop Summary," AIAA Paper 2022–3210, 2022. doi:10.2514/6.2022-3210.

[8] Frink, N. T., "Tetrahedral Unstructured Navier-Stokes Method for Turbulent Flows," *AIAA Journal*, Vol. 36, No. 11, 1998, pp. 1975–1982. https://doi.org/10.2514/2.324.

[9] Frink, N. T., Pirzadeh, S. Z., Parikh, P. C., Pandya, M. J., and Bhat, M., "The NASA Tetrahedral Unstructured Software System (TetrUSS)," *The Aeronautical Journal*, Vol. 104, No. 1040, 2000, pp. 491–499. https://doi.org/10.1017/S0001924000091995.

[10] Pandya, M. J., Frink, N. T., Ding, E., and Parlette, E., "Toward Verification of USM3D Extensions for Mixed Element Grids," *31st AIAA Applied Aerodynamics Conference*, 2013, p. 2541.

[11] Pandya, M. J., Diskin, B., Thomas, J. L., and Frink, N. T., "Assessment of USM3D Hierarchical Adaptive Nonlinear Method Preconditioners for Three-Dimensional Cases," *AIAA Journal*, 2017, pp. 3409–3424. https://doi.org/10.2514/1.J055823.

[12] Roe, P. L., "Approximate Riemann Solvers, Parameter Vectors, and Difference Schemes," *J. Comp. Phys.*, Vol. 43, 1981, pp. 357–372.

[13] Spalart, P. R., and Allmaras, S. R., "A One-Equation Turbulence Model for Aerodynamic Flows," *Recherche Aerospatiale*, Vol. 1, 1994, pp. 5–21.

[14] M. L. Shur, A. K. T., M. K. Strelets, and Spalart, P. R., "Turbulence Modeling in Rotating and Curved Channels: Assessing the Spalart-Shur Correction," *AIAA Journal*, Vol. 38, No. 5, 2000, pp. 784–792.

[15] Spalart, P. R., "Strategies for Turbulence Modelling and Simulation," *International Journal of Heat and Fluid Flow*, Vol. 21, 2000, pp. 252–263.

[16] Kleb, B., Park, M. A., Wood, W. A., Bibb, K. L., Thompson, K. B., Gomez, R. J., III, and Tesch, S. H., "Sketch-to-Solution: An Exploration of Viscous CFD with Automatic Grids," AIAA Paper 2019–2948, 2019. doi:10.2514/6.2019-2948.

[17] Park, M. A., Kleb, B., Jones, W. T., Krakos, J. A., Michal, T., Loseille, A., Haimes, R., and Dannenhoffer, J. F., III, "Geometry Modeling for Unstructured Mesh Adaptation," AIAA Paper 2019–2946, 2019. doi:10.2514/6.2019-2946.

[18] Park, M. A., Haimes, R., Wyman, N. J., Baker, P. A., and Loseille, A., "Boundary Representation Tolerance Impacts on Mesh Generation and Adaptation," AIAA Paper 2021–2992, 2021. doi:10.2514/6.2021-2992.

[19] Park, M. A., "Anisotropic Output-Based Adaptation with Tetrahedral Cut Cells for Compressible Flows," Ph.D. thesis, Massachusetts Institute of Technology, Sep. 2008. doi:1721.1/46363.

[20] Galbraith, M. C., Caplan, P. C., Carson, H. A., Park, M. A., Balan, A., Anderson, W. K., Michal, T., Krakos, J. A., Kamenetskiy, D. S., Loseille, A., Alauzet, F., Frazza, L., and Barral, N., "Verification of Unstructured Grid Adaptation Components," *AIAA Journal*, Vol. 58, No. 9, 2020, pp. 3947–3962. doi:10.2514/1.J058783.

[21] Balan, A., Park, M. A., Anderson, W. K., Kamenetskiy, D. S., Krakos, J. A., Michal, T., and Alauzet, F., "Verification of Anisotropic Mesh Adaptation for RANS Simulations over ONERA M6 Wing," *AIAA Journal*, Vol. 58, No. 4, 2020, pp. 1550–1565. doi:10.2514/1.J059158.

[22] Michal, T., Krakos, J., Kamenetskiy, D., Galbraith, M., Ursachi, C.-I., Park, M. A., Anderson, W. K., Alauzet, F., and Loseille, A., "Comparing Unstructured Adaptive Mesh Solutions for the High Lift Common Research Model Airfoil," *AIAA Journal*, Vol. 59, No. 9, 2021, pp. 3566–3584. doi:10.2514/1.J060088.

[23] Michal, T., Kamenetskiy, D., and Krakos, J., "Anisotropic Adaptive Mesh Results for the Third High Lift Prediction Workshop (HiLiftPW-3)," AIAA Paper 2018–1257, 2018. doi:10.2514/6.2018-1257.

[24] Park, M. A., Kleb, B., Anderson, W. K., Wood, S. L., Balan, A., Zhou, B. Y., and Gauger, N. R., "Exploring Unstructured Mesh Adaptation for Hybrid Reynolds-Averaged Navier-Stokes/Large Eddy Simulation," AIAA Paper 2020–1139, 2020. doi:10.2514/6.2020-1139.

[25] Balan, A., Park, M. A., Wood, S. L., Anderson, W. K., and Jacobson, K. E., "Angle-of-Attack Sweep with Mesh Adaptation for High-Lift Configurations," AIAA Paper 2022–218, 2022. doi:10.2514/6.2022-0218.

[26] Alauzet, F., and Frazza, L., "3D RANS Anisotropic Mesh Adaptation on the High-Lift Version of NASA's Common Research Model (HL-CRM)," AIAA Paper 2019–2947, 2019. doi:10.2514/6.2019-2947.

[27] Alauzet, F., Clerici, F., Loseille, A., Morisco, C. T., and Vanharen, J., "Some Progress on CFD High Lift Prediction using Metric-Based Anisotropic Mesh Adaptation," AIAA Paper 2022–388, 2022. doi:10.2514/6.2022-0388.

[28] Sukas, H., and Sahin, M., "HEMLAB Algorithm Applied to the High-Lift JAXA Standard Model," AIAA Paper 2021–1994, 2021. doi:10.2514/6.2021-1994.

[29] Alauzet, F., and Frazza, L., "Feature-Based and Goal-Oriented Anisotropic Mesh Adaptation for RANS Applications in Aeronautics and Aerospace," *Journal of Computational Physics*, Vol. 439, 2021, p. 110340. doi:10.1016/j.jcp.2021.110340.

[30] "Turbulence Modeling Resource," `https://turbmodels.larc.nasa.gov`, 2022. Accessed: 2017-03-20.

[31] Pita, C. M., and Woeber, C. D., "HLPW-4/GMGW-3: Summary of Unstructured Fixed Mesh Generation Efforts for RANS Analyses," AIAA Paper 2022–3209, 2022. doi:10.2514/6.2022-3209.

[32] Park, M. A., "HLPW-4/GMGW-3: Mesh Adaptation for RANS Technology Focus Group Workshop Summary," *AIAA AVIATION 2022 Forum*, 2022, p. 3210.